

Transient Analytical Method for Single-ended Fault Location of AC Transmission Lines Considering Fuzzy Constraints of Fault Features

Yuansheng Liang, Haoyong Chen, Jiayan Ding, Zheng Xu, Haifeng Li, and Gang Wang

Abstract—The single-ended fault location based on travelling waves (TWs) is commonly used for long-distance high-voltage AC transmission lines. However, it relies on high sampling frequency and accurate capturing of the TW head arrival time. Accordingly, this study establishes a transient analytical method for fault location based on the similarity between the transient recorded waveform and output waveforms of analytical calculation model. In the proposed method, fuzzy constraints of fault features are constructed through time-distance and waveform-scaling correlations while considering the deviation factors of the frequency-dependent wave velocity and TW head arrival time. Accordingly, the high-dimensional space of the fitting problem is transformed into a one-dimensional implicit function fitting problem containing only the fault distance, thereby enabling the waveform comparison problem to be quickly solved based on fault TW features. Under the fuzzy constraints proposed in this study, the proposed method requires only a relatively vague identification of the TW head, and the requirements for sampling frequency are also more lenient. In addition, a sliding window scheme is adopted for enhancing the TW morphology characteristics. Finally, the proposed method is tested using PSCAD, and the simulations validate the fault location accuracy of the proposed method.

Index Terms—Single-ended fault location, travelling wave, AC transmission, fuzzy constraint, analytical calculation, waveform similarity.

I. INTRODUCTION

FAST and accurate fault locations of transmission lines are crucial for the safe and reliable operation of power systems [1]–[3]. Currently, fault location methods for AC transmission line can be divided into fault-analysis-based [4]–[6] and travelling wave (TW)-based [7]–[13] methods. Fault-analysis-based methods determine the fault distance by estab-

lishing a fault location equation. These methods have the advantage of low sampling-rate dependence. However, they are susceptible to inaccuracies in extracting power-frequency phasors from fault transient data due to signal interference from the control response of power electronic devices in new power systems [14], [15]. By contrast, TW-based methods offer high fault location accuracy and are not affected by the operation mode of the system. Consequently, they are used in power systems with long-distance high-voltage transmission lines. In addition, TW-based methods require an extremely short data window and are negligibly affected by the control response. Therefore, they are better suited to the fault transient characteristics of new power systems.

TW-based methods can be classified into single- and double-ended methods. Double-ended TW-based methods utilize the difference in the TW head arrival time between the two ends for fault location and exhibit high accuracy under the conditions of high-speed sampling, data synchronization, and reliable communication. By contrast, single-ended TW-based methods require only TW information at one end of the line, making them easier to implement in engineering. However, traditional single-ended TW-based methods rely on the reflected TW at the fault point, and because of the greater distortion of the reflected TW head compared with the initial TW, it is difficult to accurately capture the arrival time of the reflected TW. This in turn affects the accuracy of the fault location. To address this issue, some researchers have focused on TW-head singularity recognition schemes based on signal processing methods. Reference [7] analyzed the accuracy of the wavelet transform in detecting TW changes, but the mother wavelet function and scaling level must be specifically selected. Reference [8] used the self-adaptive Hilbert-Huang transform to extract the TW head, thereby avoiding the difficulty in selecting the wavelet function. However, the empirical mode decomposition process under this method is susceptible to mode aliasing, which affects the accuracy of fault location. In [9], the extended Kalman filter algorithm was employed to analyze TW data and perform fault location. However, its effectiveness relies on the model parameters. In general, when the fault TW signal features are weak such as in the case of low-voltage transient values, nonmetallic faults, or remote faults, these methods that rely on TW-head calibration are susceptible to interference, reducing the reliability of these traditional single-ended

Manuscript received: April 3, 2024; revised: May 15, 2024; accepted: July 26, 2024. Date of CrossCheck: July 26, 2024. Date of online publication: August 26, 2024.

This work was supported by the Guangdong Basic and Applied Basic Research Foundation (No. 2023A1515011035).

This article is distributed under the terms of the Creative Commons Attribution 4.0 International License (<http://creativecommons.org/licenses/by/4.0/>).

Y. Liang (corresponding author), H. Chen, Z. Xu, H. Li, and G. Wang are with the School of Electric Power Engineering, South China University of Technology, Guangzhou, China (e-mail: ysliang@scut.edu.cn; 1498463892@qq.com; 732586746@qq.com; lihf@scut.edu.cn; Wangg@scut.edu.cn).

J. Ding is with the Shantou Power Supply Bureau, CSG Guangdong Power Grid Co., Ltd., Shantou, China (e-mail: djiayan@outlook.com).

DOI: 10.35833/MPCE.2024.000367



TW-based methods.

To improve the accuracy of single-ended fault locations, researchers have utilized fault characteristics such as TW dispersion to enhance the feature information for fault locations. References [10] and [11] used continuous wavelet transform and S-transform to extract the fault information matrix of the transient signal. They then estimated the fault distance by comparing the information matrix with offline datasets. Fault transient travelling wave (FTTW) signal datasets require the use of electromagnetic transient simulation software to simulate various fault scenarios. However, in AC transmission systems, the FTTW waveform varies depending on factors such as fault inception angle, fault resistance, and system operation mode. Therefore, comprehensive coverage of all fault conditions using only simulations is challenging. In [12] and [13], artificial intelligence (AI) model was employed to map the tags of datasets to determine the fault position. However, AI methods require extensive simulations to generate samples and reconstruct models to supply samples for new scenarios. In addition, the network hyperparameters must be adjusted during the training process. These issues limit the application of AI methods to fault locations. Therefore, some researchers have introduced complex-domain analytical calculations into fault feature analysis, which are commonly used in modular multilevel converter based high-voltage direct current systems [16]-[19]. Reference [16] proposed a descending-order adaptive frequency-partitioned fitting algorithm for frequency responses, which enables the fast calculation of the frequency-dependent parameters of high-voltage direct current (HVDC) transmission lines. Reference [17] proposed a transient analytical calculation method for multiterminal hybrid HVDC systems that can replace simulation software to achieve fast and accurate transient calculations. References [18] and [19] visually demonstrated the effects of fault factors on fault features using an established fault transient analytical calculation method, providing a theoretical basis for their research on protection principles and fault location methods. However, no studies have been conducted on the application of complex-domain analytical calculation models for fault locations in AC transmission systems.

Under the description of complex-domain fault boundary conditions for complex-domain analytical calculation models of AC transmission systems, the fault inception angle of the fault point differs from the reference angle of the measurement point due to the delay caused by TW propagation. This angle deviation is related to the fault distance, propagation velocity, and TW head arrival time, and it is difficult to accurately measure the moment at which the initial TW reaches the measurement point. Consequently, the output waveform of the complex-domain analytical calculation exhibits significant errors without constraints on the phasor-angle deviation for the delay in TW propagation. Therefore, fitting a complex-domain analytical calculation model to fault recorded data is a challenging task for AC transmission systems. In some fault cases under the waveform matching method, the fault feature waveforms of TW may be sparsely scattered over the timeline. Differential features are masked directly

using the waveform similarity index. This drawback is not conducive to accurate fault locations.

Therefore, based on the complex-domain analytical calculation model, this study proposes a transient analytical method for single-end fault location of AC transmission lines considering fuzzy constraints of fault features. The main contributions of the proposed method are as follows.

1) The fuzzy constraints of fault features are constructed through time-distance and waveform-scaling correlations while considering the deviation factors of the frequency-dependent wave velocity and TW head arrival time. A characteristic sensitivity analysis reveals that under the maximum total angular deviation of the fuzzy constraints, the sinusoidal variation difference is small. Thus, the proposed fuzzy constraints effectively suppress errors caused by unmeasurable factors, and when combined with linear least-squares fitting, the high-dimensional space of the fitting problem can be transformed into a one-dimensional implicit function-fitting problem that includes only the fault distance.

2) A window sliding method for enhancing the waveform similarity features is proposed. First, the length of the sliding window is shortened to make the waveform similarity features more focused on the TW features and to suppress the effects of feature sparsity. Second, the window sliding method enhances the time-axis dimension of the fault characteristics and increases the sensitivity of the TW morphology characteristics associated with the fault distance.

The remainder of this paper is organized as follows. Section II presents the complex-domain analytical calculation model for FTTW. Section III analyzes the characteristic sensitivities of all fault factors on the FTTW waveform based on the analytical calculation model. Section IV presents the derivation of the fuzzy constraints of fault features that correlate with the analytical calculation model and recorded data. Section V describes the transient analytical method for single-ended fault location based on TW morphology characteristics. Section VI describes the validation of the effectiveness of the proposed method through case studies. Finally, conclusions are drawn in Section VII.

II. COMPLEX-DOMAIN ANALYTICAL CALCULATION MODEL FOR FTTW

A. Frequency-dependent Nodal Impedance Correlation Model of Power Grid

After a fault occurs on a transmission line during the transient initial stage, the fault current exhibits multi-characteristic frequency signals. Accordingly, the frequency-dependent characteristics of the analytical calculation model for FTTW must be considered. The frequency-dependent parameters of transmission lines such as the per-unit-length series impedance and parallel admittance, are typically derived using a vector fitting algorithm with a rational function approximation [20]. This derivation is based on the detailed parameters of transmission lines.

The transmission line model of the complex-domain analytical calculation model for the FTTW can then be con-

structured based on the long-line equation with frequency-dependent parameters [21] as follows:

$$\begin{bmatrix} I_J(s) \\ I_K(s) \end{bmatrix} = \begin{bmatrix} y_s(s) & y_m(s) \\ y_m(s) & y_s(s) \end{bmatrix} \begin{bmatrix} U_J(s) \\ U_K(s) \end{bmatrix} \quad (1)$$

$$\begin{cases} y_s(s) = \gamma(s) \mathbf{T} \gamma(s)^{-1} \coth(\gamma(s)l) \mathbf{T}^{-1} \\ y_m(s) = -\gamma(s) \mathbf{T} \gamma(s)^{-1} \operatorname{csch}(\gamma(s)l) \mathbf{T}^{-1} \end{cases} \quad (2)$$

$$\gamma(s) = \sqrt{\mathbf{T}^{-1} y(s) z(s) \mathbf{T}} \quad (3)$$

where $I_J(s)$ and $I_K(s)$ are the complex-domain currents at terminals J and K of the line, respectively; $U_J(s)$ and $U_K(s)$ are the complex-domain voltages at terminals J and K of the line, respectively; $y_s(s)$ and $y_m(s)$ are the complex-domain self-admittance and mutual admittance of the line, respectively; l is the length of the line; \mathbf{T} is the Clarke transformation matrix; $\gamma(s)$ is the per-unit-length propagation coefficient of the line in the form of a complex domain; and $y(s)$ and $z(s)$ are the per-unit-length parallel admittance and series impedance of the line, respectively.

Then, based on the augmented incidence matrix of the faulty and adjacent lines and the equivalent system parameters of the adjacent remote nodes, the complex-domain nodal admittance matrix of the transmission system is established and inverted into the complex-domain nodal impedance matrix of the transmission system. Thus, if a fault occurs at a fault distance d_f from the terminal J of the line, the complex-domain nodal impedance matrix of the extended fault node network can be determined by appending the tree and link branches to the initial complex-domain nodal impedance matrix, which is set as $\mathbf{Z}(s)|_{d=d_f}$ in this study. Consequently, selecting a different d_f changes the self-impedance of the fault point and its mutual impedance at both terminals of the line.

B. Complex-domain Short-circuit Current Calculation Model

For a fault port f , the time-domain model of the fault excitation voltage source can be expressed as:

$$\Delta u_{f\Phi}(t) = U_f \sin(\alpha(t - t_0) + \theta_{f\Phi}) \varepsilon(t - t_0) \quad (4)$$

where Δu_f is the fault excitation voltage source; the subscript Φ represents each phase; U_f is the voltage amplitude at the fault point before the fault occurs; α is the power angular frequency; t_0 is the time when a short circuit occurs; θ_f is the fault inception angle; and $\varepsilon(t - t_0)$ is a unit-step signal.

The time-domain models of fault boundary conditions for different fault types can be established as follows.

1) Single-phase-to-ground short circuit:

$$\begin{cases} u_{ff\Phi_f}^{(1)}(t) = -\Delta u_{f\Phi_f}(t) + R_f i_{ff\Phi_f}^{(1)}(t) \\ i_{ff\Phi_{\bar{f}}}^{(1)}(t) = i_{ff\Phi_{\bar{f}}}^{(0)}(t) = 0 \end{cases} \quad (5)$$

where u_{ff} and i_{ff} are the voltage and outflow-node current at fault port f in the fault additional network, respectively; the subscript Φ_f represents the fault phase; the subscripts $\Phi_{\bar{f}_1}$ and $\Phi_{\bar{f}_2}$ represent two non-fault phases; the superscript (1) represents the fault type of single-phase-to-ground short-circuit; and R_f is the fault resistance.

2) Phase-to-phase short circuit:

$$\begin{cases} u_{ff\Phi_{\bar{f}_1}}^{(2)}(t) - u_{ff\Phi_{\bar{f}_2}}^{(2)}(t) = -\Delta u_{f\Phi_{\bar{f}_1}}(t) + \Delta u_{f\Phi_{\bar{f}_2}}(t) + R_f i_{ff\Phi_{\bar{f}_1}}^{(2)}(t) \\ i_{ff\Phi_f}^{(2)}(t) = 0 \\ i_{ff\Phi_{\bar{f}_1}}^{(2)}(t) = -i_{ff\Phi_{\bar{f}_2}}^{(2)}(t) \end{cases} \quad (6)$$

where the subscripts $\Phi_{\bar{f}_1}$ and $\Phi_{\bar{f}_2}$ represent two fault phases; the subscript Φ_f represents the non-fault phase; and the superscript (2) represents the fault type of phase-to-phase short circuit.

3) Two-phase-to-ground short circuit:

$$\begin{cases} u_{ff\Phi_{\bar{f}_1}}^{(1,1)}(t) = -\Delta u_{f\Phi_{\bar{f}_1}}(t) + R_f (i_{ff\Phi_{\bar{f}_1}}^{(1,1)}(t) + i_{ff\Phi_{\bar{f}_2}}^{(1,1)}(t)) \\ u_{ff\Phi_{\bar{f}_2}}^{(1,1)}(t) = -\Delta u_{f\Phi_{\bar{f}_2}}(t) + R_f (i_{ff\Phi_{\bar{f}_1}}^{(1,1)}(t) + i_{ff\Phi_{\bar{f}_2}}^{(1,1)}(t)) \\ i_{ff\Phi_f}^{(1,1)}(t) = 0 \end{cases} \quad (7)$$

where the superscript (1,1) represents the fault type of two-phase-to-ground short circuit.

4) Three-phase short circuit:

$$u_{ff\Phi}^{(3)}(t) = -\Delta u_{f\Phi}(t) + R_f i_{ff\Phi}^{(3)}(t) \quad (8)$$

where the superscript (3) represents the fault type of three-phase short circuit.

The complex-domain expression of fault boundary conditions can be established by applying a Laplace transformation to the electrical quantities of each phase at the fault port. By utilizing symmetrical component transformation and constructing the connection of sequence networks, this study derives the complex-domain expression of the short-circuit current at the fault port as:

$$-I_{ff\Phi}^{(type)}(s) = -\frac{U_f e^{-st_0}}{2j(s - j\alpha)} \frac{m_1^{(type)} e^{j\theta^{(type)}}}{Z_{ff(1)}(s) + Z_{\Delta}^{(type)}(s)} - \frac{U_f e^{-st_0}}{2j(s + j\alpha)} \frac{m_2^{(type)} e^{-j\theta^{(type)}}}{Z_{ff(1)}(s) + Z_{\Delta}^{(type)}(s)} \quad (9)$$

where I_{ff} is the complex-domain expression of i_{ff} ; the superscript (type) represents the fault type; $Z_{ff(1)}(s)$ is the positive-sequence complex-domain self-impedance of the fault port in $\mathbf{Z}(s)|_{d=d_f}$; and Z_{Δ} , m_1 , m_2 , and θ are the parameters related to the fault types, with their expressions summarized in Supplementary Material A Table SAI.

C. Analytical Calculation Model for FTTW

The complex-domain expression of the transient current at terminal J can be obtained through the use of $\mathbf{Z}(s)|_{d=d_f}$ and $I_{ff}^{(type)}$ as:

$$\begin{cases} I_J^{(type)}(s) = y_s(s) U_J^{(type)}(s) + y_m(s) U_K^{(type)}(s) \\ U_J^{(type)}(s) = Z_{Jf}(s) I_{ff}^{(type)}(s) \\ U_K^{(type)}(s) = Z_{JK}(s) I_{ff}^{(type)}(s) \end{cases} \quad (10)$$

where $Z_{Jf}(s)$ and $Z_{JK}(s)$ are the mutual impedance elements between nodes f and J (or K) in $\mathbf{Z}(s)|_{d=d_f}$, respectively.

The solution to (10) in the complex domain can be converted into a numerical solution in the time domain by applying a numerical inverse Laplace transform as [22]:

$$\begin{cases} f(k\Delta t) = \text{Re} \left(\frac{2}{N\Delta t} e^{ck\Delta t + jk\frac{\pi}{N}} \sum_{m=0}^{N-1} F(c + j\omega_m) \sigma(\omega_m) e^{j\frac{2\pi mk}{N}} \right) \\ \omega_m = (2m+1) \frac{\pi}{N\Delta t} \\ c = \frac{2\ln N}{N\Delta t} \end{cases} \quad (11)$$

where Δt is the time step of the numerical solution in the time domain; N is the number of samples; k is the sampling point and $k=0, 1, \dots, N-1$; ω_m is the corresponding discrete angular frequency for the calculation; c is a stability constant; $F(\cdot)$ is a concrete causal complex-domain function; $f(\cdot)$ is the corresponding numerical solution of $F(s)$ in the time domain; and $\sigma(\cdot)$ is the Hanning function.

The calculation for the current FTTW from (1)-(11) can be expressed in an implicit function form as:

$$\mathbf{i}_{JK} = F_{f\text{type}}(U_f, t_0, \theta_f, R_f, d_f) \quad (12)$$

where \mathbf{i}_{JK} is the numerical solution of the line-terminal fault current; and $F_{f\text{type}}(\cdot)$ is the implicit function of calculation for the current FTTW.

According to the established analytical calculation model, if the variables in (12) are equal to those under the actual fault conditions, the output waveform of the analytical calculation model should be consistent with the recorded FTTW waveform.

D. Effective Time Window of Analytical Calculation Model for FTTW

When the complete transmission system is modeled in detail, the output waveform of the proposed complex-domain analytical calculation model is fully consistent with the simulation waveform. However, from the practical engineering perspective, this modeling is not feasible. Typically, only the target line and its adjacent lines can be mathematically modeled in detail. In addition, the impedance parameter of the system changes during operation, which can result in calculation errors in the reflectivity between adjacent lines and remote buses. Figure 1 shows the difference between the output waveform of the analytical calculation model and the simulation waveform when detailed mathematical modeling is performed only on the target line and its adjacent lines.

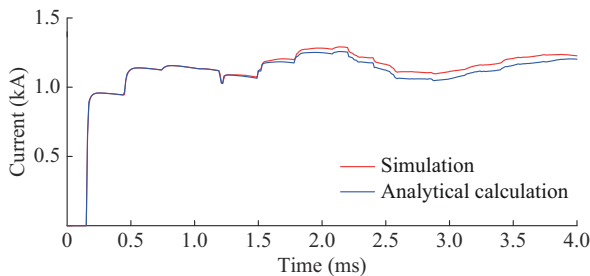


Fig. 1. Comparison between output waveform of analytical calculation model and simulation waveform.

The fault example presented in Fig. 1 is a single-phase-grounding fault with a fault resistance of 100Ω and a fault inception angle of 90° at 44 km. As Fig. 1 illustrates, the output waveform of the analytical calculation model and the

simulation waveform are highly consistent within milliseconds before the arrival of the externally reflected TW. However, after the reflected TW arrives from the far end of the non-detailed modeled lines, the amplitude of the FTTW begins to deviate. Therefore, the length of the accurately modeled adjacent lines determines the effective length of the time window of the analytical calculation model.

III. CHARACTERISTIC SENSITIVITY ANALYSIS BASED ON ANALYTICAL CALCULATION MODEL

The fault factor variables in (12), including the pre-fault voltage amplitude at the fault point U_f , fault occurrence time t_0 , fault inception angle θ_f , fault resistance R_f , and fault distance d_f , are all unknown when a fault occurs. Conducting a calculation from these five dimensions is extremely time-consuming and not easily feasible. Therefore, this section presents a sensitivity analysis of these unknown variables in the analytical calculation model to explore fault characteristic description methods that enhance the sensitivity of d_f while reducing the sensitivity of other variables.

A. Pre-fault Voltage Amplitude

The magnitude of the steady-state short-circuit current is determined by U_f . The amplitude of the pre-fault voltage at the line terminal can be obtained from the recorded data. However, U_f cannot be estimated in advance because of the unknown fault location.

Equations (9) and (10) show that the complex-domain expression of the fault current at the line-terminal measurement point is linearly proportional to U_f . Because the deviation in the pre-fault voltage amplitude is insignificant, the output waveforms of the analytical calculation model exhibit high longitudinal similarity under different U_f values, as shown in Fig. 2(a). By employing similarity evaluation indexes such as the longest common subsequence method and cosine similarity, the feature differences in the proportional scaling of FTTW magnitudes can be effectively reduced.

B. Fault Occurrence Time and Fault Inception Angle

Although t_0 and θ_f are closely related variables, their relationship is not well-defined until the fault distance is confirmed. To analyze the effects of their deviation values on the output waveforms, different values are selected for these two variables, and analytical calculations are conducted to observe the resulting waveforms.

When θ_f is held constant and t_0 is changed, based on (4), (9), and (10), the output waveforms of the analytical calculation model shift along the time axis, as shown in Fig. 2(b). This deviation in t_0 can be considered as an error in the start-up time of the recorded data.

However, when t_0 is held constant (where the reference zero time is used as an example) and θ_f is changed, the output waveforms of the analytical calculation model are shown in Fig. 2(c)-(f). Figure 2(c) shows that, even though the TW head arrival time is approaching, significant differences exist in the shape of the output waveforms under the superposition of steady-state sine waves at different phasor angles, which can be better understood via (4).

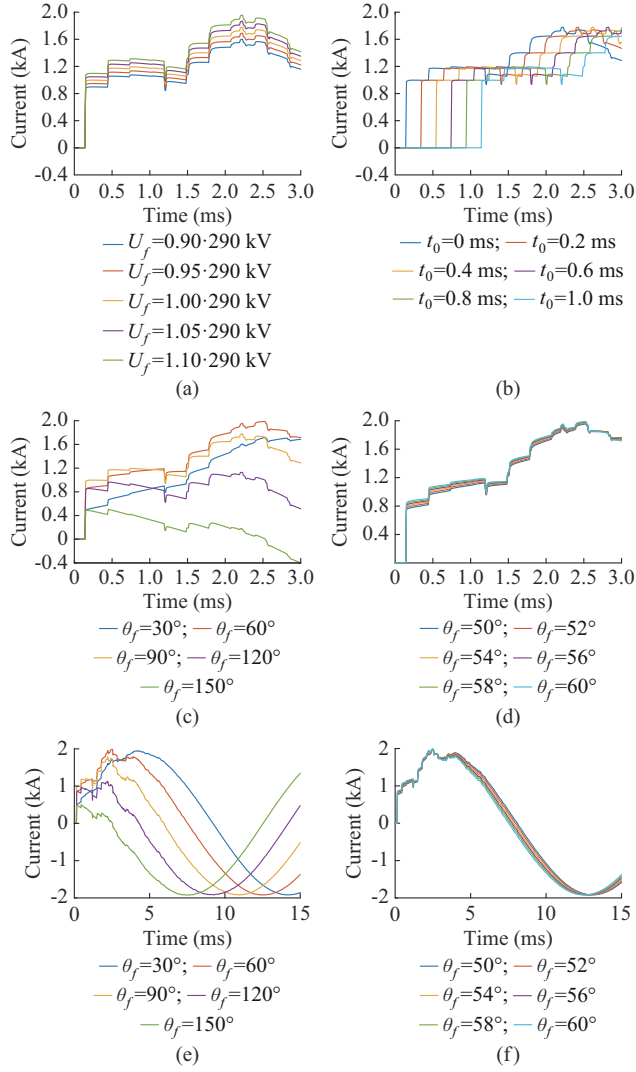


Fig. 2. Comparison of current FTTW waveforms under different values of each variable related to fault excitation source. (a) U_f . (b) t_0 . (c) θ_f ($\Delta\theta_f > 30^\circ$ within 3 ms). (d) θ_f ($\Delta\theta_f < 10^\circ$ within 3 ms). (e) θ_f ($\Delta\theta_f > 30^\circ$ within 15 ms). (f) θ_f ($\Delta\theta_f < 10^\circ$ within 15 ms).

After TW attenuation, the differences among these output waveforms include only the differences in sine waves with different phasor angles, as shown in Fig. 2(e). When θ_f is only slightly different, as the phasor angles of fault excitation sources are relatively close, the output waveforms of the analytical calculation model are highly consistent, as shown in Fig. 2(d) and (f).

C. Fault Resistance

When a fault point contains R_f , the value of R_f determines the refractive and reflective indices of the TW passing through the fault point. This directly affects the amplitudes of TW at different orders. Based on the assumption that the n^{th} arriving TW undergoes p_1 reflections and p_2 refractions at the fault point and based on the fact that the degree of propagation loss is related only to the propagation distance, the influence coefficient of R_f on the amplitudes of TW at different orders can be derived as:

$$K_{R_f, n} = \frac{1}{Z_c + 2R_f} \left(\frac{-Z_c}{Z_c + 2R_f} \right)^{p_1} \left(\frac{2R_f}{Z_c + 2R_f} \right)^{p_2} \quad (13)$$

where K_{R_f} is the influence coefficient of R_f on the amplitude of TW; the subscript n represents the order of TW; Z_c is the wave impedance of the fault line; and p_1 and p_2 are the reflection and refraction times of the TW passing through the fault point, respectively.

From (13), it can be observed that the effect of R_f on the amplitudes of TW at different orders is nonlinear. The relationship curve between K_{R_f} and R_f/Z_c for TW at different orders (TW1-TW5) is shown in Fig. 3(a). As the TW arrives at different time, the difference in the current FTTW waveforms gradually increases over time due to the varying values of R_f , as depicted in Fig. 3(b). Therefore, the output waveforms for different values of R_f are not a cluster of proportionally scaled curves, which fundamentally differ from the deviation of U_f . In addition, existing waveform similarity indicators cannot eliminate these differences. Thus, the variations in the values of the aforementioned variables will result in differences in the similarity indexes of the output waveforms of analytical calculation model, thereby increasing the complexity of the fault location searching model.

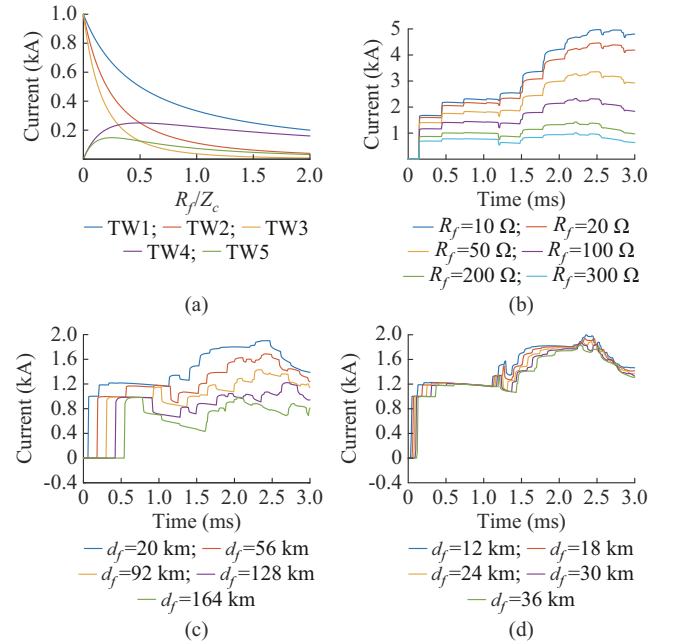


Fig. 3. Effect of R_f on amplitudes of TW at different orders and comparison of current FTTW waveforms with different fault resistances and fault distances. (a) Effect of R_f on amplitudes of TW at different orders. (b) R_f . (c) d_f ($\Delta d_f > 36$ km). (d) d_f ($\Delta d_f < 6$ km).

D. Fault Distance

The most critical variable in determining fault locations is d_f . From (9) and (10), when different values of d_f are selected in the analytical calculation model, the output waveforms exhibit variations in amplitude and time differences for TW at different orders, as shown in Fig. 3(c) and (d). As Fig. 3(c) shows, significant differences are observed in the arrival time of TW at different orders when a substantial difference

exists in the variable d_f used in the analytical calculation model. In addition, the overall amplitude of the current FTTW waveform differs significantly, resulting in variations in the waveform similarity. As Fig. 3(d) shows, when the difference in d_f is small, the amplitude difference between the FTTW waveforms is also relatively small, indicating that the feature difference in the overall FTTW waveform similarity is less sensitive. However, with respect to TW morphology, the differences in TW waveform similarity are significant. Therefore, improving the morphology characterization of the TW is crucial for enhancing the sensitivity of d_f in fault location methods.

IV. FUZZY CONSTRAINTS OF FAULT FEATURES CORRELATING WITH ANALYTICAL CALCULATION MODEL AND RECORDED DATA

The output waveform of the analytical calculation model depends on several factors, including the chosen fault distance, fault resistance, and fault excitation source. Given the numerous variables involved, establishing correlation constraints among the recorded data, fault distance, fault excitation source signal, and fault resistance is critical. A single-ended fault location model is then constructed using a comparison index between the fault recorded data and the output waveforms of the analytical calculation model.

Because of the effects of factors such as the recording sampling interval and inaccurate calibration of the initial TW head arrival time, constructing fuzzy constraints that consider errors in the transient recorded data, fault distance, fault excitation source, and fault resistance is necessary.

A. Fuzzy Constraint of Time-distance Correlation

The instantaneous voltage and current before and after the fault can be obtained from the recorded data. When the single-ended positive-sequence voltage and current phasors prior to the fault are utilized, the pre-fault voltage phasor expression related to variable d_f can be established using the long-line equation:

$$\dot{U}_f(d_f) = \dot{U}_J \cosh(\gamma_\alpha d_f) - \dot{I}_J Z_c \sinh(\gamma_\alpha d_f) \quad (14)$$

where \dot{U}_J and \dot{I}_J are the power-frequency sinusoidal voltage phasor and current phasor measured at terminal J at the moment of abrupt waveform, respectively; γ_α is the per-unit-length power-frequency propagation coefficient of the transmission line; and \dot{U}_f is the corresponding power-frequency sinusoidal voltage phasor of the fault point. The amplitude and phasor angle of \dot{U}_f are described as:

$$\begin{cases} U_f(d_f) = |\dot{U}_f(d_f)| \\ \varphi_f(d_f) = \arg(\dot{U}_f(d_f)) \end{cases} \quad (15)$$

In fact, the reference zero time of fault recording is usually the starting moment when the initial TW reaches the measurement point, meaning that the fault occurrence time should precede the reference zero time by a corresponding delay in the TW propagation. Therefore, to obtain the phasor angle of the fault excitation voltage at the fault point, the propagation delay of the fault voltage phasor derived from

(14) must be compensated for:

$$\theta_f(d_f) = \varphi_f(d_f) - \alpha \frac{d_f}{v} + \Delta\theta(\varphi_f, v) \quad (16)$$

where v is the propagation velocity of TW; and $\Delta\theta$ is the total angular deviation caused by the detection error and frequency-dependent wave velocity deviation.

In (16), $\alpha d_f/v$ denotes the delay angle of TW propagation. Because $\Delta\theta$ is unknown, it is considered a fuzzy variable, and its error must be further evaluated. Considering the actual engineering scenarios, for example, if the length of the AC transmission line does not exceed 300 km, the ultimate propagation velocity of TW does not exceed 3×10^5 km/s, the sampling rate of the TW recording ranges from 20 to 100 kHz, and the deviation of the corresponding identification result of initial TW head arrival time is not greater than 50-90 μ s, then the corresponding deviation of $\Delta\theta$ does not exceed 0.9° to 1.62° . According to the result shown in Fig. 2(f), because the sinusoidal variation difference in the output waveform of the analytical calculation model is very small under the maximum degree of $\Delta\theta$, the total angular deviation can be ignored. With $\Delta\theta(\varphi_f, v)$ of (16) ignored and with (16) substituted into (4), the expression of the fault excitation source associated with the pre-fault voltage phasor and fault distance can be approximated as:

$$\begin{cases} \Delta u_f(t) \approx U_f \sin\left(\alpha(t-t_0) + \varphi_f - \alpha \frac{d_f}{v}\right) \varepsilon(t-t_0) \\ t_0 = -\frac{d_f}{v} \end{cases} \quad (17)$$

Thus, the variable U_f is precalculated from (15), and both t_0 and θ_f are related to (17) with respect to d_f . Therefore, the current FTTW from (12) can be rewritten as a function of R_f and d_f as follows:

$$\begin{cases} \dot{i}_{JK}(R_f, d_f) = F_{type}(U_f, t_0, \theta_f, R_f, d_f) \\ U_f(d_f) = \left| \dot{U}_J \cosh(\gamma_\alpha d_f) - \dot{I}_J Z_c \sinh(\gamma_\alpha d_f) \right| \\ t_0(d_f) = -\frac{d_f}{v} \\ \theta_f(d_f) \approx \arg(\dot{U}_J \cosh(\gamma_\alpha d_f) - \dot{I}_J Z_c \sinh(\gamma_\alpha d_f)) - \alpha \frac{d_f}{v} \end{cases} \quad (18)$$

B. Correlation Constraint on Fault Distance and Fault Resistance for Fault Characterization Enhancement

According to the analysis of the correlation between the output waveform of the analytical calculation model and R_f as presented in Section III-C, the amplitudes of TW at different orders show different proportions of scaling effects under different values of R_f . From (13), for the first-order TW in which $n=1$ and $p_1=p_2=0$, the influence coefficient of its amplitude on R_f can be derived as:

$$K_{R_f,1} = \frac{1}{Z_c + 2R_f} \quad (19)$$

Therefore, the relationship between the analytical outputs of different resistances in the shape of the first-order TW is proportional and can be described as:

$$\frac{i_{JK,t}(R_f, d_f)}{i_{JK,t}(R_{assume}, d_f)} = \frac{\frac{1}{Z_c + 2R_f}}{\frac{1}{Z_c + 2R_{assume}}} = \frac{Z_c + 2R_{assume}}{Z_c + 2R_f} \quad \forall t \in T_1 \quad (20)$$

where R_{assume} is the assumed fault resistance that can be set as any constant; T_1 is the time window of the initial TW; and $i_{JK,t}$ is the numerical solution of the line-terminal fault current in the t^{th} time series of the initial TW.

If d_f is consistent with the actual fault distance, from (18), the scaling relationship between the recorded waveform and analytical output in the shape of the first-order TW can be described as:

$$i_{JKrec,t} \cong i_{JK,t}(R_f, d_f) \approx i_{JK,t}(R_{assume}, d_f) \frac{Z_c + 2R_{assume}}{Z_c + 2R_f} \quad (21)$$

where $i_{JKrec,t}$ is the recorded data of the line-terminal fault current.

Thus, R_f can be solved by converting the coincidence degree of (20) into a linear least-squares fitting of each time series of the first-order TW as:

$$R_f(d_f) = \frac{(Z_c + 2R_{assume}) \sum_{t \in T_1} i_{JKrec,t} i_{JK,t}(R_{assume}, d_f)}{2 \sum_{t \in T_1} i_{JKrec,t}^2} - \frac{Z_c}{2} \quad (22)$$

If the selected d_f in (22) deviates from the actual fault distance, the resulting R_f deviates from the actual value. This enhances the correlation between the analytical output waveforms and the variable d_f , which helps to improve the variable sensitivity of d_f . Therefore, when (22) is substituted into (18), the analytical calculation model for the single-ended fault location can be transformed into a function that contains only the variable d_f as follows:

$$\begin{cases} i_{JK}(d_f) = F_{f\text{type}}(U_f, t_0, \theta_f, R_f, d_f) \\ U_f(d_f) = \left| \dot{U}_j \cosh(\gamma_a d_f) - \dot{I}_j Z_c \sinh(\gamma_a d_f) \right| \\ t_0(d_f) = -\frac{d_f}{v} \\ \theta_f(d_f) \approx \arg(\dot{U}_j \cosh(\gamma_a d_f) - \dot{I}_j Z_c \sinh(\gamma_a d_f)) \phi_f - \alpha \frac{d_f}{v} \\ R_f(d_f) = \frac{(Z_c + 2R_{assume}) \sum_{t \in T_1} i_{JKrec,t} i_{JK,t}(R_{assume}, d_f)}{2 \sum_{t \in T_1} i_{JKrec,t}^2} - \frac{Z_c}{2} \end{cases} \quad (23)$$

Under (23), a series of undetermined variables d_f is scanned to obtain the unique corresponding output waveforms of the analytical calculation model. These waveforms are then matched with the recorded waveforms, as shown in Fig. 4.

Clearly, within a 1 km range, distinguishable morphological differences exist in the output waveforms for different d_f . Consequently, the fault location can be determined by a single scan of d_f and by calculating the waveform similarity index for waveform matching. The cosine similarity index is chosen as the waveform similarity index in this study [23]:

$$S_{\cos}(i_{JKrec,t}, i_{JK,t}) = \frac{\sum_{t \in T_2} i_{JKrec,t} i_{JK,t}}{\sqrt{\sum_{t \in T_2} i_{JKrec,t}^2} \sqrt{\sum_{t \in T_2} i_{JK,t}^2}} \quad (24)$$

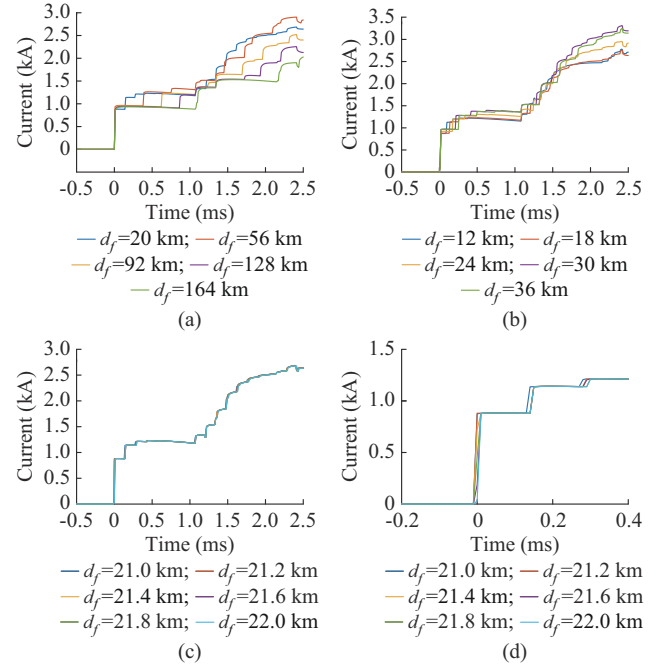


Fig. 4. Comparison of current FTTW waveforms corresponding to different values of d_f . (a) d_f ($\Delta d_f > 36$ km). (b) d_f ($\Delta d_f < 6$ km). (c) d_f ($\Delta d_f < 0.2$ km). (d) Localized enlarged view ($\Delta d_f < 0.2$ km).

where T_2 is the time window for calculating the waveform similarity index.

V. TRANSIENT ANALYTICAL METHOD FOR SINGLE-ENDED FAULT LOCATION BASED ON MORPHOLOGY CHARACTERISTICS

Figure 4(c) and (d) demonstrates that when d_f deviates from the actual distance by less than 1 km, the analytical output waveforms remain highly similar. This difference is primarily observed in the surges of TW at different orders. However, this similarity in the waveform does not contribute to accurate fault location. To address this issue, the time window length is reduced to distinguish the morphology characteristics of the wave head, which is similar to the effect of amplifying the waveform along the time axis. In this study, the time window length of the waveform similarity assessment is shortened, and a sliding window scheme is adopted to fully utilize all FTTW characteristics within the effective data window.

The similarity feature map is expanded into three dimensions as the data window slides along the time axis. The highest similarity index results can only be maintained during the window sliding process if the value of d_f is consistent with the actual fault distance. However, if the value of d_f differs from the actual fault distance, the similarity index results exhibit a low similarity valley at the data segments of the respective TW head arrival, resulting in a “cliff” phenomenon. This phenomenon enhances the feature differences in the waveform similarity for different fault distances during the waveform matching process, as illustrated in Fig. 5. The theoretical consistency between the value of d_f and the actual fault distance is crucial for maintaining high similarity

results during the window sliding process. The flowchart of the transient analytical method for single-ended fault location is presented in Fig. 6.

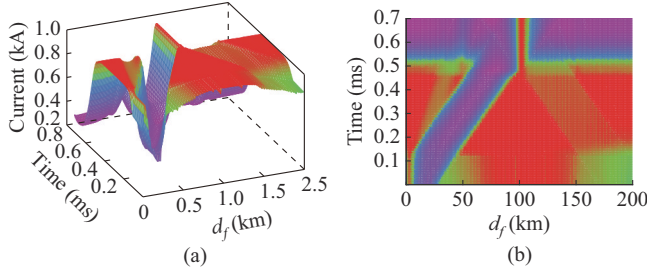


Fig. 5. Three-dimensional presentation of cosine similarity index results based on sliding windows with short data window. (a) Isometric view. (b) Top view.

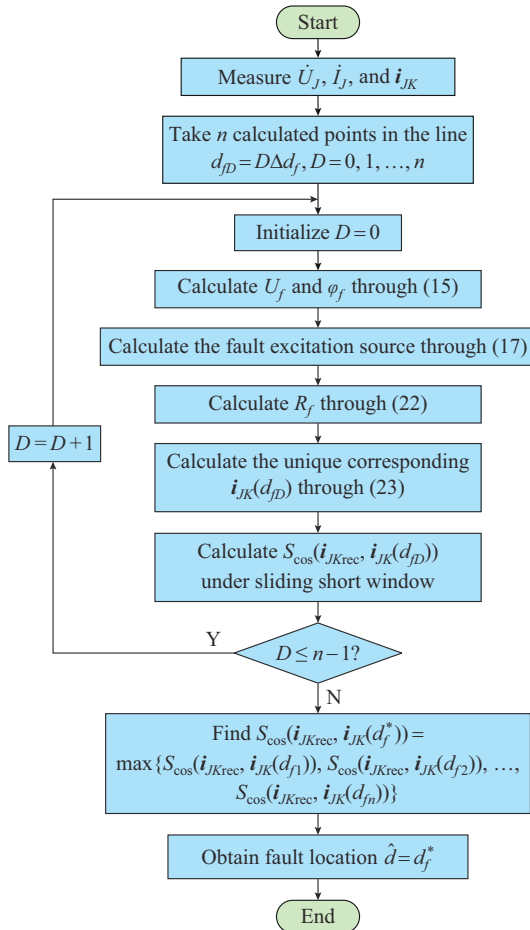


Fig. 6. Flowchart of transient analytical method for single-ended fault location.

For transient fault location methods, using a shorter data window results in harsher fault location requirements. To locate faults accurately, ensuring that the recorded data exhibit significant TW morphology characteristics at any distance is crucial. This can be accomplished by using an effective data window for a fault location that includes at least two TWs. Notably, the second TW, which reaches the line-terminal measurement point, experiences the longest delay when a fault occurs in the middle of the line. Considering redundancy, we set the minimum length of the data window used in

the proposed method to at least $1.2l/v$.

VI. SIMULATION VERIFICATION AND RESULT ANALYSIS

A. Simulation Case

To evaluate the effectiveness of the proposed method, electromagnetic transient simulation models of a 500 kV AC transmission system are constructed using PSCAD/EMTDC, which include a simplified double-circuit network topology (topology 1) and an IEEE 30-node network topology (topology 2), as shown in Fig. 7(a) and (b), respectively. The parameters of these two topologies are presented in Supplementary Material A Fig. SA1. Due to engineering constraints, only the measured transmission line and its adjacent lines are accurately modeled based on the measured line length. The accurately modeled transmission line is highlighted in red in Fig. 7.

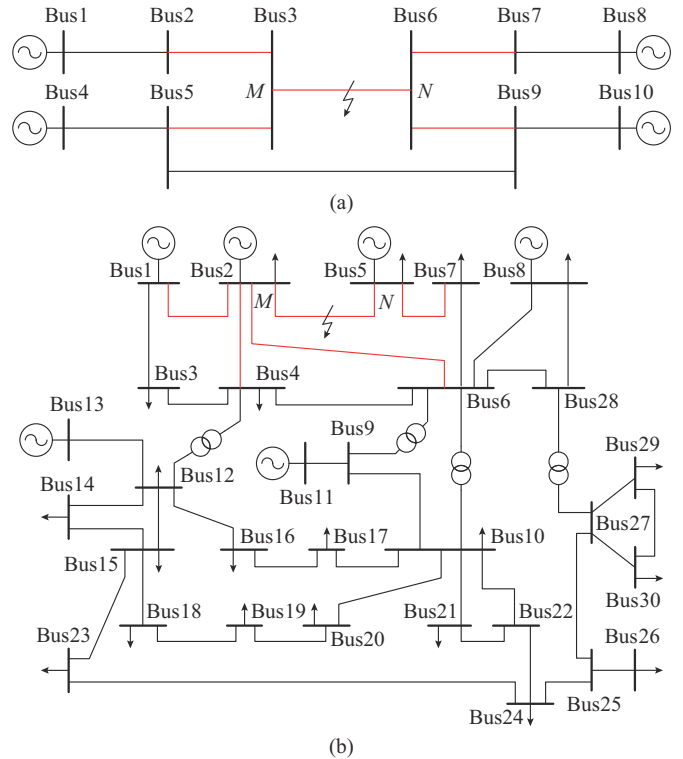


Fig. 7. Schematics of network topology in PSCAD. (a) Schematic of simplified double-circuit network topology. (b) Schematic of IEEE 30-node network topology.

For simulation purposes, different fault types, fault inception angles, and fault resistances are set at various positions along the line. The pre-fault voltage and current signals as well as the current recorded data are collected at terminal M at a sampling frequency of 100 kHz. Because the measured line has a total length of 200 km, a redundant data window is set to be 0.8 ms after the recording starts. The variable d_f is scanned for analytical calculations from terminals M to N along the transmission line.

B. Analysis of Results

1) Typical Fault Case Study

Fault location methods based on waveform matching rely

mainly on the morphology characteristics of the wave head. When a fault occurs in the middle or near the end of the line, TW exhibits a sparse or dense distribution on the time axis. In addition, when a fault occurs at a lower fault inception angle and higher fault resistance, the characteristics of TW are relatively weak. Therefore, the location results for three typical fault cases are demonstrated.

1) In the case of a fault occurring in the middle of the line, the TW head arrival time interval is long, and the TW morphology characteristics are sparsely distributed on the time axis. As an example, a single-phase-to-ground fault with a fault resistance of 200 Ω and a fault inception angle of 90° occurring at 102.46 km is selected, and the fault location process is shown in Fig. 8. First, the recorded waveform data within 0.8 ms following the start of recording at terminal *M* are obtained, as shown by the solid line in Fig. 8(a).

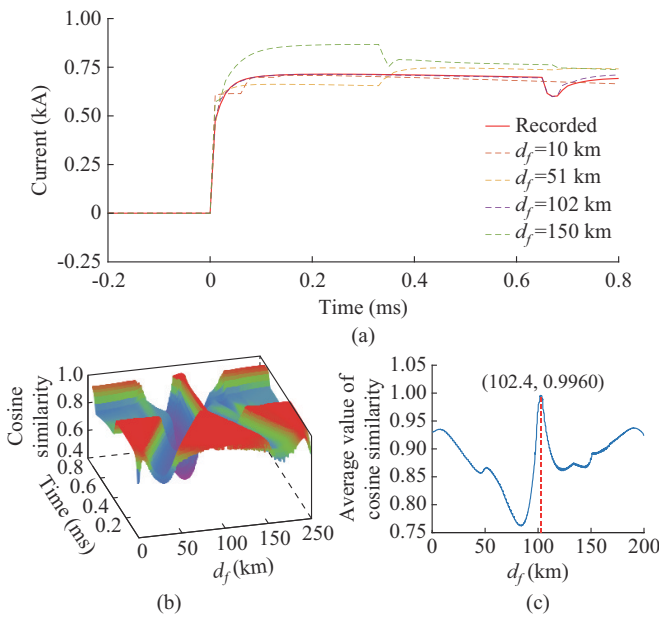


Fig. 8. Fault location process ($R_f=200\ \Omega$ and $d_f=102.46\ \text{km}$). (a) Simulated and partially analyzed FTTW waveforms. (b) Cosine similarity index with sliding window data. (c) Average value of cosine similarity index.

The time-domain FTTW waveforms at different fault distances can then be obtained using (23), as shown by dashed lines in Fig. 8(a). Next, the cosine similarity index is used to compare the analyzed waveforms of each fault distance with the recorded data, as shown in Fig. 8(b). The average value of the cosine similarity index is shown in Fig. 8(c), where the location of the fault point is determined, which coincides with the actual fault distance. When a fault occurs near the middle of the line, the selected redundant effective time window ensures that the second TW reaches the measurement point, thus ensuring the applicability of the proposed method.

2) In the case of a fault near the end of the line, multiple TW reflections occur in a short period, and the TW morphology characteristics are concentrated in the first half of the time axis. As an example, a single-phase-to-ground fault with a fault resistance of 20 Ω and a fault inception angle of 90° occurring at 10.04 km is selected, and the fault location process is shown in Fig. 9. Under this fault condition, the

proposed method can still accurately determine the fault location.

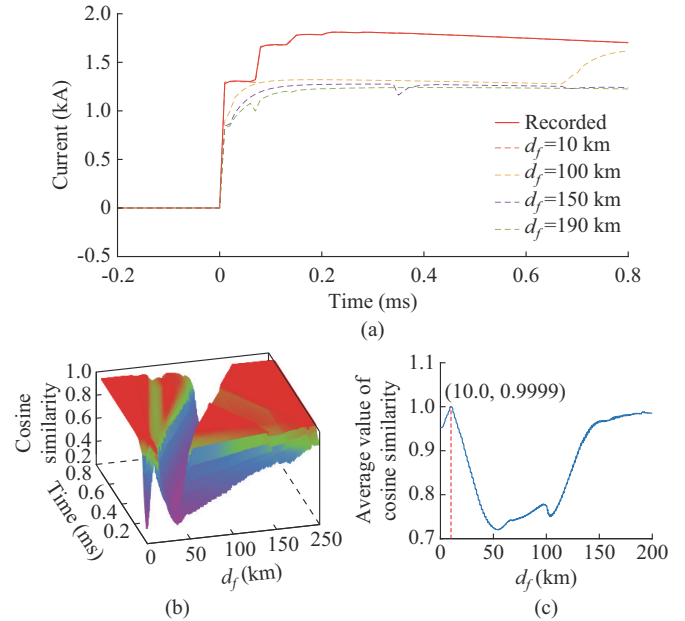


Fig. 9. Fault location process ($R_f=20\ \Omega$ and $d_f=10.04\ \text{km}$). (a) Simulated and partially analyzed FTTW waveforms. (b) Cosine similarity index with sliding window data. (c) Average value of cosine similarity index.

3) In the case of a fault occurring under extreme conditions, the TW morphology characteristics become even weaker due to the effects of propagation losses. As an example, a single-phase-to-ground fault with a fault resistance of 400 Ω and a fault inception angle of 6° occurring at 180.51 km is selected, and the fault location process is shown in Fig. 10.

Under this fault condition, the proposed method can still accurately determine the fault location.

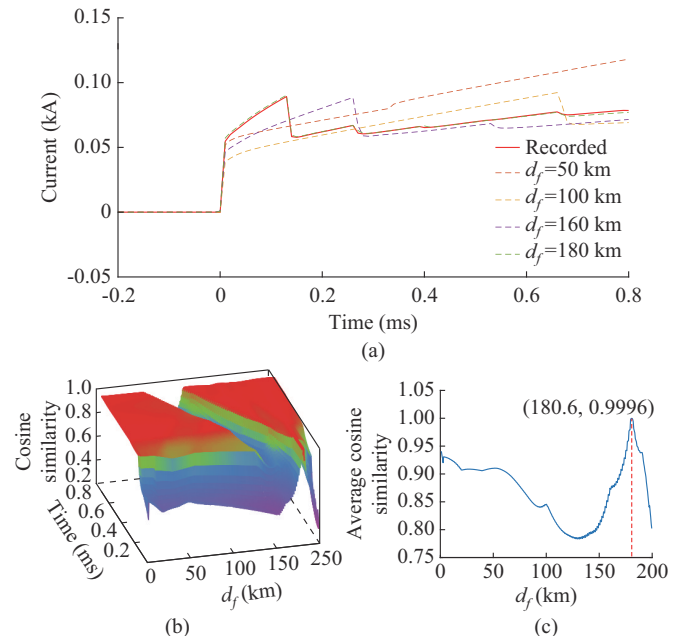


Fig. 10. Fault location process ($R_f=400\ \Omega$ and $d_f=180.51\ \text{km}$). (a) Simulated and partially analyzed FTTW waveforms. (b) Cosine similarity index with sliding window data. (c) Average value of cosine similarity index.

2) Effectiveness of Fault Location

This study conducted multiple simulations to evaluate the effectiveness of the proposed method. The simulations involve different fault distances, inception angles, resistances, and types. The specific values for each fault factor are as follows. The actual fault distances are distributed along the entire line with values of 5.89, 10.04, 20.39, 30.35, 50.28, 75.42, 102.46, 149.67, and 190.72 km. The fault inception angles are 90°, 60°, 30°, and 6°. The fault resistance values are 0, 20, and 200 Ω. The fault types include four types of AC transmission line short-circuit faults. Tables I-IV list the location results of the proposed method under different fault conditions. In these tests, the average time consumed for a fault location calculation does not exceed 10 s with the i5-12400 processor.

TABLE I
LOCATION RESULTS FOR DIFFERENT ACTUAL FAULT DISTANCES UNDER METALLIC SINGLE-PHASE-TO-GROUND FAULTS WITH FAULT INCEPTION ANGLE OF 90°

| Topology | Actual fault distance (km) | Location result (km) | Error (km) |
|----------|----------------------------|----------------------|------------|
| 1 | 5.89 | 5.9 | +0.01 |
| | 10.04 | 10.1 | +0.06 |
| | 20.39 | 20.4 | +0.01 |
| | 30.35 | 30.3 | -0.05 |
| | 50.28 | 50.3 | +0.02 |
| | 75.42 | 75.4 | -0.02 |
| | 102.46 | 102.5 | +0.04 |
| | 149.67 | 149.6 | -0.07 |
| | 190.72 | 190.7 | -0.02 |
| 2 | 5.89 | 5.9 | +0.01 |
| | 10.04 | 10.1 | +0.06 |
| | 20.39 | 20.5 | +0.11 |
| | 30.35 | 30.3 | -0.05 |
| | 50.28 | 50.3 | +0.02 |
| | 75.42 | 75.3 | -0.12 |
| | 102.46 | 102.5 | +0.04 |
| | 149.67 | 149.6 | -0.07 |
| | 190.72 | 190.6 | -0.12 |

Results in Tables I-IV indicate that the proposed method is minimally affected by various factors and is applicable to different topological structures. The maximum error observed does not exceed 0.3 km, with a relative error not exceeding 0.15%, which demonstrates a high accuracy level.

C. Method Adaptability Analysis

To further verify the adaptability and superiority of the proposed method, tests are conducted on other influencing factors, excluding the fault factors, using the fault data of topology 1.

1) Effects of Deviations of Transmission Line Parameters

The proposed method requires a detailed mathematical model of the target line and its adjacent lines. Based on the potential geometric deviations between the established model and the actual transmission line, tests are performed to analyze the effects of deviations of transmission line parameters. The corresponding location results are listed in Table V.

TABLE II
LOCATION RESULTS FOR DIFFERENT FAULT INCEPTION ANGLES UNDER METALLIC SINGLE-PHASE-TO-GROUND FAULTS

| Topology | Actual fault distance (km) | Fault inception angle (°) | Location result (km) | Error (km) |
|----------|----------------------------|---------------------------|----------------------|------------|
| 1 | 10.04 | 90 | 10.1 | +0.06 |
| | | 60 | 10.1 | +0.06 |
| | | 30 | 10.1 | +0.06 |
| | | 6 | 9.9 | -0.14 |
| | 30.35 | 90 | 30.3 | -0.05 |
| | | 60 | 30.3 | -0.05 |
| | | 30 | 30.3 | -0.05 |
| | | 6 | 30.2 | -0.15 |
| | 102.46 | 90 | 102.5 | +0.04 |
| | | 60 | 102.5 | +0.04 |
| | | 30 | 102.5 | +0.04 |
| | | 6 | 102.3 | -0.16 |
| 2 | 10.04 | 90 | 10.1 | +0.06 |
| | | 60 | 10.1 | +0.06 |
| | | 30 | 10.1 | +0.06 |
| | | 6 | 9.9 | -0.14 |
| | 30.35 | 90 | 30.3 | -0.05 |
| | | 60 | 30.3 | -0.05 |
| | | 30 | 30.3 | -0.05 |
| | | 6 | 30.2 | -0.15 |
| | 102.46 | 90 | 102.5 | +0.04 |
| | | 60 | 102.5 | +0.04 |
| | | 30 | 102.5 | +0.04 |
| | | 6 | 102.6 | +0.14 |

TABLE III
LOCATION RESULTS FOR DIFFERENT FAULT RESISTANCES UNDER SINGLE-PHASE-TO-GROUND FAULTS WITH FAULT INCEPTION ANGLE OF 90°

| Topology | Actual fault distance (km) | Fault resistance (Ω) | Location result (km) | Error (km) | |
|----------|----------------------------|----------------------|----------------------|------------|-------|
| 1 | 5.89 | 0 | 5.9 | +0.01 | |
| | | 20 | 5.9 | +0.01 | |
| | | 200 | 5.9 | +0.01 | |
| | 75.42 | 0 | 75.4 | -0.02 | |
| | | 20 | 75.4 | -0.02 | |
| | | 200 | 75.4 | -0.02 | |
| | 149.67 | 0 | 149.6 | -0.07 | |
| | | 20 | 149.6 | -0.07 | |
| | | 200 | 149.6 | -0.07 | |
| | 2 | 5.89 | 0 | 5.9 | +0.01 |
| | | | 20 | 5.9 | +0.01 |
| | | | 200 | 6.0 | +0.11 |
| 75.42 | | 0 | 75.3 | -0.12 | |
| | | 20 | 75.3 | -0.12 | |
| | | 200 | 75.3 | -0.12 | |
| 149.67 | | 0 | 149.6 | -0.07 | |
| | | 20 | 149.6 | -0.07 | |
| | | 200 | 149.5 | -0.17 | |

TABLE IV
LOCATION RESULTS FOR DIFFERENT FAULT TYPES UNDER METALLIC
FAULTS WITH FAULT INCEPTION ANGLE OF 90°

| Topology | Actual fault distance (km) | Fault type | Location result (km) | Error (km) |
|----------|----------------------------|------------|----------------------|------------|
| 1 | 20.39 | AG | 20.4 | +0.01 |
| | | BC | 20.5 | +0.11 |
| | | BCG | 20.4 | +0.01 |
| | | ABC | 20.5 | +0.11 |
| | 50.28 | AG | 50.3 | +0.02 |
| | | BC | 50.2 | -0.08 |
| | | BCG | 50.3 | +0.02 |
| | | ABC | 50.3 | +0.02 |
| | 190.72 | AG | 190.7 | -0.02 |
| | | BC | 190.8 | +0.08 |
| | | BCG | 190.6 | -0.12 |
| | | ABC | 190.7 | -0.02 |
| 2 | 20.39 | AG | 20.5 | +0.11 |
| | | BC | 20.5 | +0.11 |
| | | BCG | 20.4 | +0.01 |
| | | ABC | 20.4 | +0.01 |
| | 50.28 | AG | 50.3 | +0.02 |
| | | BC | 50.3 | +0.02 |
| | | BCG | 50.4 | +0.12 |
| | | ABC | 50.3 | +0.02 |
| | 190.72 | AG | 190.6 | -0.12 |
| | | BC | 190.5 | -0.22 |
| | | BCG | 190.5 | -0.22 |
| | | ABC | 190.6 | -0.12 |

Note: AG, BC, BCG, and ABC represent single-phase-to-ground, phase-to-phase, two-phase-to-ground, and three-phase short-circuit faults, respectively.

TABLE V
LOCATION RESULTS FOR DIFFERENT DEVIATIONS IN LINE PARAMETERS
UNDER SINGLE-PHASE-TO-GROUND FAULTS WITH FAULT RESISTANCE
OF 20Ω AND FAULT INCEPTION ANGLE OF 30°

| Actual fault distance (km) | Deviation degree (%) | Location result (km) | Error (km) |
|----------------------------|----------------------|----------------------|------------|
| 30.35 | +5 | 30.0 | -0.35 |
| | +3 | 30.2 | -0.15 |
| | 0 | 30.3 | -0.05 |
| | -3 | 30.6 | +0.25 |
| | -5 | 30.8 | +0.45 |
| 149.67 | +5 | 150.1 | +0.43 |
| | +3 | 149.9 | +0.23 |
| | 0 | 149.6 | -0.07 |
| | -3 | 149.5 | -0.17 |
| | -5 | 149.2 | -0.47 |

Table V shows that when a deviation exists between the established model and the actual transmission line, as the deviation degree increases, the errors of the location results increase slightly. When the deviation degree is within $\pm 5\%$, the maximum fault location error does not exceed 0.5 km, with a relative error not exceeding 0.25%, which is within

an acceptable range. Therefore, the proposed method has a certain degree of tolerance to deviations in the transmission line parameters.

2) Effects of Noise Interference

Regarding noise interference, white noise with different signal-to-noise ratios (SNRs) is added to the original signal to verify the effectiveness of the proposed method. The corresponding location results are listed in Table VI.

TABLE VI
LOCATION RESULTS FOR DIFFERENT NOISES UNDER METALLIC
SINGLE-PHASE-TO-GROUND FAULTS WITH FAULT INCEPTION ANGLE OF 6°

| Actual fault distance (km) | SNR (dB) | Location result (km) | Error (km) |
|----------------------------|----------|----------------------|------------|
| 20.39 | | 20.4 | +0.01 |
| | 70 | 20.4 | +0.01 |
| | 60 | 20.4 | +0.01 |
| | 50 | 20.6 | +0.21 |
| | 40 | 20.8 | +0.41 |
| 102.46 | | 102.4 | -0.06 |
| | 70 | 102.4 | -0.06 |
| | 60 | 102.4 | -0.06 |
| | 50 | 102.2 | -0.26 |
| | 40 | 102.0 | -0.46 |

As Table VI shows, as the SNR decreases, the morphology characteristics of the actual transient fault waveforms are significantly affected, which can lead to increased errors in fault location. When the SNR is in the range of 40-70 dB, the proposed method can still achieve accurate and reliable fault locations with a maximum fault location error not exceeding 0.5 km and a relative error not exceeding 0.25%.

3) Effects of Sampling Frequency

The implementation of the fault location method depends on the on-site fault locators, and the sampling frequency is a critical parameter of the fault locator. Therefore, testing the effects of different sampling frequencies on the proposed method is essential. The corresponding location results are presented in Table VII.

TABLE VII
LOCATION RESULTS FOR DIFFERENT SAMPLING FREQUENCIES UNDER
SINGLE-PHASE-TO-GROUND FAULTS WITH FAULT RESISTANCE OF
 200Ω AND FAULT INCEPTION ANGLE OF 6°

| Actual fault distance (km) | Sampling frequency (kHz) | Location result (km) | Error (km) |
|----------------------------|--------------------------|----------------------|------------|
| 75.42 | 20 | 76.5 | +1.08 |
| | 50 | 75.2 | -0.22 |
| | 100 | 75.4 | -0.02 |
| | 500 | 75.4 | -0.02 |
| | 1000 | 75.4 | -0.02 |
| 190.72 | 20 | 191.5 | +0.78 |
| | 50 | 190.8 | +0.08 |
| | 100 | 190.8 | +0.08 |
| | 500 | 190.7 | -0.02 |
| | 1000 | 190.7 | -0.02 |

As Table VII shows, increasing the sampling frequency does not significantly affect the location results of typical faults. This is attributed to the fuzzy constraints in this study, which enhance the correlation between the fault TW features and fault distance. However, when the sampling frequency is too low, such as 20 kHz, the maximum fault location error exceeds 1 km with a relative error exceeding 0.5%.

This study presents a transient analytical method based on TW morphology characteristics. In extreme fault situations in which the fault TW features are weak, such as when the fault inception angle is close to zero, it is not conducive to accurate location by the proposed method.

However, increasing the sampling frequency can enrich the fault TW features within the data window. Therefore, tests of the proposed method under extreme fault conditions at different sampling frequencies are conducted, and the corresponding results are presented in Table VIII.

TABLE VIII
ERRORS IN EXTREME CASES AT DIFFERENT SAMPLING FREQUENCIES
UNDER SINGLE-PHASE-TO-GROUND FAULTS WITH FAULT
RESISTANCE OF 600 Ω OCCURRING AT 50.28 KM

| Sampling frequency (kHz) | Fault inception angle ($^{\circ}$) | Location result (km) | Error (km) |
|--------------------------|--------------------------------------|----------------------|------------|
| 50 | 6 | 50.6 | +0.32 |
| | 4 | 51.1 | +0.82 |
| | 2 | 51.1 | +0.82 |
| 100 | 6 | 50.5 | +0.22 |
| | 4 | 50.6 | +0.32 |
| | 2 | 50.8 | +0.52 |
| 500 | 6 | 50.3 | +0.02 |
| | 4 | 50.3 | +0.02 |
| | 2 | 50.6 | +0.32 |
| 1000 | 6 | 50.3 | +0.02 |
| | 4 | 50.3 | +0.02 |
| | 2 | 50.4 | +0.12 |

As Table VIII shows, when the sampling frequency is set to be 50 kHz, the fault location error significantly increases when the fault inception angle decreases from 6 $^{\circ}$ to 2 $^{\circ}$. And when the sampling frequency is increased to 1000 kHz, the proposed method can accurately determine the fault location under the fault inception angle of 2 $^{\circ}$. Therefore, raising the sampling frequency can effectively enhance the adaptability of the proposed method to extreme fault conditions.

4) Comparative Analysis with Existing Single-end Fault Location Methods

To verify the superiority of the proposed method, tests are conducted to compare the proposed method and other fault location methods, including the wavelet transform-based fault location method (method 1) [10] and the neural network-based fault location method (method 2) [19], with these designations and their corresponding location results listed in Table IX.

Table IX shows that the proposed method effectively utilizes the TW morphology characteristics regarding only the fault distance under fuzzy constraints of fault features, which

leads to improved fault location accuracy as compared with other fault location methods.

TABLE IX
LOCATION RESULTS FOR DIFFERENT LOCATION METHODS UNDER
METALLIC SINGLE-PHASE-TO-GROUND FAULTS WITH FAULT
INCEPTION ANGLE OF 60 $^{\circ}$

| Actual fault distance (km) | Method | Location result (km) | Error (km) |
|----------------------------|----------|----------------------|------------|
| 50.28 | Proposed | 50.3 | +0.02 |
| | 1 | 50.8 | +0.52 |
| | 2 | 51.3 | +1.02 |
| 102.46 | Proposed | 102.5 | +0.04 |
| | 1 | 103.2 | +0.74 |
| | 2 | 103.3 | +0.84 |
| 149.67 | Proposed | 149.6 | -0.07 |
| | 1 | 149.3 | -0.37 |
| | 2 | 150.5 | +0.83 |

VII. CONCLUSION

In this study, a transient analytical method for single-ended fault location of AC transmission lines considering fuzzy constraints of fault features is proposed. Complex-domain analytical calculations are first applied to AC transmission systems, and a mathematical analytical calculation model is then established between the single-ended FTTW of an AC transmission line fault and various fault conditions. Fuzzy constraints of fault features are also proposed for fault excitation sources, fault resistances, and fault distances. Fuzzy constraints transform the high-dimensional space of the fitting problem into a one-dimensional implicit function fitting problem containing only the fault distance. To further improve the similarity features between the output waveforms of the analytical calculation model and fault recorded waveforms at fault points, a waveform similarity index under a short sliding window is proposed. Simulation results demonstrate that this index effectively differentiates the fault point and is unaffected by fault resistance. In addition, the proposed method accounts for fuzzy constraints by considering errors in the TW head arrival time. Consequently, precise identification of the TW head is not required. Another advantage is that the proposed method does not require a pre-established FTTW dataset because the analytical calculation model establishes a correlation between the fault distance and recorded data. Thus, the proposed method can adapt to different system operation modes and various fault situations within a short data window based on FTTW.

REFERENCES

- [1] C. M. Furse, M. Kafal, R. Razzaghi *et al.*, "Fault diagnosis for electrical systems and power networks: a review," *IEEE Sensors Journal*, vol. 21, no. 2, pp. 888-906, Jan. 2021.
- [2] H. A. Abdel-Ghany, A. M. Azmy, and A. M. Abeid, "A general traveling-wave-based scheme for locating simultaneous faults in transmission lines," *IEEE Transactions on Power Delivery*, vol. 35, no. 1, pp. 130-139, Feb. 2020.
- [3] L. F. Ugarte, M. C. de Almeida, and L. H. T. Bandória, "Fault location approach to distribution networks based on custom state estimator," *Journal of Modern Power Systems and Clean Energy*, vol. 11,

- no. 6, pp. 1878-1889, Nov. 2023.
- [4] Y. Liang, J. Ding, H. Li *et al.*, "Transmission line frequency-domain fault location method based on the phasor-time space curve characteristics that considers decaying DC deviation," *International Journal of Electrical Power & Energy Systems*, vol. 142, pp. 108-308, Nov. 2022.
- [5] C. G. Arsoniadis and V. C. Nikolaidis, "Fault location method for overhead feeders with distributed generation units based on direct load flow approach," *Journal of Modern Power Systems and Clean Energy*, vol. 12, no. 4, pp. 1135-1146, Jul. 2024.
- [6] L. Ji, X. Tao, Y. Fu *et al.*, "A new single ended fault location method for transmission line based on positive sequence superimposed network during auto-reclosing," *IEEE Transactions on Power Delivery*, vol. 34, no. 3, pp. 1019-1029, Jun. 2019.
- [7] M. Parsi, P. Crossley, P. L. Dragotti *et al.*, "Wavelet based fault location on power transmission lines using real-world travelling wave data," *Electric Power Systems Research*, vol. 186, pp. 1-10, Sept. 2020.
- [8] K. Duan, Y. Fan, Y. Wang *et al.*, "A traveling wave ranging method for a DC line based on wave velocity compensation and fault distance approaching its real value gradually," *Power System Protection and Control*, vol. 49, no. 11, pp. 70-78, Jun. 2021.
- [9] Y. Xi, Z. Li, X. Zeng *et al.*, "Fault location based on travelling wave identification using an adaptive extended Kalman filter," *IET Generation, Transmission & Distribution*, vol. 12, no. 6, pp. 1314-1322, Feb. 2018.
- [10] F. Deng, X. Zeng, X. Tang *et al.*, "Travelling-wave-based fault location algorithm for hybrid transmission lines using three-dimensional absolute grey incidence degree," *International Journal of Electrical Power & Energy Systems*, vol. 114, p. 105306, Jan. 2020.
- [11] Z. Li, J. Liu, Y. Xi *et al.*, "Fault location method for distribution network based on transient waveform correlation," *Automation of Electric Power Systems*, vol. 44, no. 21, pp. 72-79, Nov. 2020.
- [12] J. Hu, W. Hu, J. Chen *et al.*, "Fault location and classification for distribution systems based on deep graph learning methods," *Journal of Modern Power Systems and Clean Energy*, vol. 11, no. 1, pp. 35-51, Jan. 2023.
- [13] F. Deng, Y. Zhong, Z. Zeng *et al.*, "A single-ended fault location method for transmission line based on full waveform feature extraction of traveling waves," *IEEE Transactions on Power Delivery*, vol. 38, no. 4, pp. 2585-2595, Aug. 2023.
- [14] H. Xie, M. Jiang, D. Zhang *et al.*, "IntelliSense technology in the new power systems," *Renewable and Sustainable Energy Reviews*, vol. 177, p. 113229, May 2023.
- [15] Q. Chen, P. Qiu, Y. Lu *et al.*, "Research on the photovoltaic project access system scheme of Yang Shan Island," *Energy Reports*, vol. 8, pp. 106-112, Nov. 2022.
- [16] J. Guo, G. Wang, D. Zeng *et al.*, "Descending-order adaptive frequency-partitioned fitting algorithm of frequency responses for short-circuit calculation on HVDC transmission lines," *Proceedings of the CSEE*, vol. 36, no. 13, pp. 3534-3545, Jul. 2016.
- [17] H. Li, C. Xu, Y. Liang *et al.*, "Fault transient calculation method for multi-terminal hybrid HVDC systems considering control characteristics of converter station," *Proceedings of the CSEE*, vol. 43, no. 4, pp. 1426-1438, Feb. 2023.
- [18] Z. Huang, Y. Liang, H. Li *et al.*, "Analytical calculation method of traveling wave for three-terminal hybrid DC system considering characteristics of T-connect bus," *Automation of Electric Power Systems*, vol. 44, no. 17, pp. 136-144, Apr. 2020.
- [19] Y. Liang, L. Jiang, H. Li *et al.*, "Fault analysis and traveling wave protection based on phase characteristics for hybrid multiterminal HVDC systems," *IEEE Journal of Emerging and Selected Topics in Power Electronics*, vol. 10, no. 1, pp. 575-588, Feb. 2022.
- [20] B. Gustavsen and A. Semlyen, "Rational approximation of frequency domain responses by vector fitting," *IEEE Transactions on Power Delivery*, vol. 14, no. 3, pp. 1052-1061, Jul. 1999.
- [21] A. S. Morched, J. H. Ottevangers, and L. Marti, "Multi-port frequency dependent network equivalents for the EMTP," *IEEE Transactions on Power Delivery*, vol. 8, no. 3, pp. 1402-1412, Jul. 1993.
- [22] P. Gómez and F. A. Uribe, "The numerical Laplace transform: an accurate technique for analyzing electromagnetic transients on power system devices," *International Journal of Electrical Power & Energy Systems*, vol. 31, no. 2, pp. 116-123, Feb. 2009.
- [23] X. Wei, X. Wang, J. Gao *et al.*, "Faulty feeder detection for single-phase-to-ground fault in distribution networks based on transient energy and cosine similarity," *IEEE Transactions on Power Delivery*, vol. 37, no. 5, pp. 3968-3979, Oct. 2022.

Yuansheng Liang received the B.S. and Ph.D. degrees in electrical engineering from the South China University of Technology, Guangzhou, China, in 2003 and 2008, respectively. He is currently working as an Associate Professor at the School of Electric Power Engineering, South China University of Technology. His research interests include protection and control, fault analysis and location of power systems, and collaborative optimization of active distribution networks.

Haoyong Chen received the B.S. degree in electrical engineering from the South China University of Technology, Guangzhou, China, in 2022. He is currently pursuing the M.S. degree in electrical engineering at the South China University of Technology. His research interests include fault characteristic analysis and protection of new power systems.

Jiayan Ding received the B.S. and M.S. degrees in electrical engineering from South China University of Technology, Guangzhou, China, in 2020 and 2023, respectively. She is currently working at the Shantou Power Supply Bureau, CSG Guangdong Power Grid Co., Ltd., Shantou, China. Her research interests include protection and control of power systems.

Zheng Xu received the B.S. and M.S. degrees in electrical engineering from South China University of Technology, Guangzhou, China, in 2021 and 2024, respectively. She is currently working at the State Grid Sichuan Electric Power Company, Chengdu, China. Her research interests include fault characteristic analysis and protection of new power systems.

Haifeng Li received the B.S., M.S., and Ph.D. degrees in electrical engineering from the South China University of Technology, Guangzhou, China, in 1998, 2001, and 2004, respectively. He is currently working as a Professor at the School of Electric Power Engineering, South China University of Technology. His research interest includes power system protection using high-voltage direct current technology.

Gang Wang received the B.S. degree in electrical engineering from Tianjin University, Tianjin, China, in 1988, the M.S. degree in electrical engineering from Taiyuan Institute of Technology, Taiyuan, China, in 1991, and the Ph.D. degree in electrical engineering from Tianjin University, in 1994. He is currently working as a Professor at the School of Electric Power Engineering, South China University of Technology, Guangzhou, China, where he is also the Director of the Power Engineering and Technology Research and Development Center. His research interests include power system protection and control, fault analysis, power system planning and reliability, and high-voltage direct current technology.